

Sea ice concentration variability over the Southern Ocean and its impact on precipitation in southeastern South America

Ramiro Saurral,* Vicente Barros and Inés Camilloni

Centro de Investigaciones del Mar y la Atmósfera (CIMA/CONICET-UBA), UMI IFAECI/CNRS and Departamento de Ciencias de la Atmósfera y los Océanos (FCEN-UBA), Buenos Aires, Argentina

ABSTRACT: This article quantifies the relationship between sea ice cover (SIC) on the Southern Ocean and precipitation and river discharges over southeastern and eastern South America. The period of analysis covers from 1981 to 2008 and includes monthly mean data of SIC over the Ross, Amundsen–Bellingshausen and Weddell Seas, as well as atmospheric variables and discharges of selected rivers in eastern South America. To isolate the effect of known modes of climate variability on SIC, the signals of El Niño–Southern Oscillation and the Southern Annual Mode are removed from all time series through regression analysis. Composites of precipitation differences over South America reveal a pattern of enhanced rainfall activity over the South Atlantic Convergence Zone (SACZ) in summer (JFM) when SIC is above average particularly over the Weddell Sea area, while winter (ASO) SIC anomalies show negative and significant correlations with rainfall over much of South America. Moisture fluxes patterns in summer reveal increased moisture transport towards the SACZ region and decreased low-level jet activity (and precipitation) over northern Argentina. In particular a large dry bias over southeastern South America associated to positive SIC anomalies on the Weddell Sea in September is shown to impact the discharges of the Uruguay and Iguazú Rivers, with the largest effects found two months after the SIC anomaly (November). Although less robust, a relationship with the Paraná River is also found. These results suggest that increased SIC over the Weddell Sea during September can help to forecast drier conditions particularly on the Uruguay basin and somewhat wetter conditions in the SACZ region within the following season.

KEY WORDS sea ice variability; South American climate; precipitation; rivers

Received 1 November 2012; Revised 10 September 2013; Accepted 13 September 2013

1. Introduction

The Southern Hemisphere (SH) is characterized by large water masses that account for nearly 80% of the total surface of the hemisphere and an annual mean area of 12 million km² (about 6%) of sea covered by ice. Thus, variability on sea surface temperature (SST) and sea ice cover (SIC) may play a significant role in the atmospheric circulation of the region (Kushnir *et al.*, 2002; Brayshaw *et al.*, 2008). Although many studies treat SIC variability as primarily driven by the atmospheric and oceanic circulation and not vice versa (Deser *et al.*, 2000; Renwick, 2002; Zhang, 2007; Stammerjohn *et al.*, 2008), other authors showed that changes in SIC also impact the atmospheric circulation (Justino and Peltier, 2006; Matthewman and Magnusdottir, 2011). Kidston *et al.* (2011) recently performed simulations with an atmospheric general circulation model modifying the latitudinal extent of the sea ice edge (SIE) on the SH and found that the position

of the SIE has a noticeable impact on the location of the mid-latitude jet stream, especially in the cold season. Raphael *et al.* (2011) found that during those austral summers when SIC is at its largest extent there is a marked alteration in the high- and mid-latitude SH circulation and showed that SIC variability also exerts an influence in the phase and amplitude of the Southern Annular Mode (SAM), the leading mode of atmospheric variability south of 20°S.

In the last decades there have been large changes in the atmospheric circulation and related mean temperature around many parts of Antarctica. The Antarctic Peninsula is the SH high latitude region where the largest positive temperature trends have been observed (Vaughan *et al.*, 2003; Steig *et al.*, 2009; O'Donnell *et al.*, 2011). This warming, mostly explained by the significant strengthening of the SAM (Thompson *et al.*, 2000; Marshall, 2003), may have played a role in the collapse of several ice shelves and could be associated with sea ice loss in the surrounding seas (Turner *et al.*, 2005; Turner and Overland, 2009; Screen and Simmonds, 2012). Independently on the main driver behind these variations – either greenhouse gases concentration increases (Cai *et al.*, 2003), stratospheric ozone depletion due to enhanced aerosol

*Correspondence to: R. I. Saurral, Centro de Investigaciones del Mar y la Atmósfera, Int. Guiraldes 2160, Ciudad Universitaria, Pab. 2 (C1428EGA), Buenos Aires, Argentina. E-mail: saurral@cima.fcen.uba.ar

concentration (Thompson and Solomon, 2002; Turner *et al.*, 2009) or natural forcing (Marshall *et al.*, 2004) –, they have influenced both the SST and SIC fields around Antarctica.

Precipitation variability in South America is known to be highly dependent on the phase and strength of El Niño–Southern Oscillation or ENSO (Ropelewski and Halpert, 1987; Grimm *et al.*, 2000), and on the amplitude and phase of the SAM. Silvestri and Vera (2003) showed that precipitation over southeastern South America (SESA) in winter and spring is strongly modulated by the SAM, although this relationship was found to have varied along the second half of the 20th century (Silvestri and Vera, 2009). However, until now the potential relationships (if any) existing between SIC around Antarctica and South American climate are not clear.

The scope of this article is to analyse the covariability between SIC and precipitation anomalies over South America. Three distinct regions around Antarctica are selected and analysed individually: Ross Sea, Amundsen–Bellingshausen Sea and Weddell Sea and their relationships with patterns of rainfall anomalies are assessed. An analysis of long-term trends in SIC and their possible links to precipitation variability over South America is also performed. The article is organized as follows: Section 2 includes the description of SIC, precipitation, streamflow and circulation variables datasets along with the methodologies. Section 3 includes the analysis on SIC and precipitation variability and covariability. The main atmospheric circulation anomalies related to SIC variability are included in Section 4. Section 5 includes a discussion of potential seasonal predictability of rainfall and river discharges for selected basins arising from the SIC–precipitation analysis. Conclusions are presented in Section 6.

2. Data and methodology

SIC data was taken from the HadISST dataset (Rayner *et al.*, 2003 and updates) for the whole SH and precipitation data was obtained from CMAP (Xie and Arkin, 1997) covering the South American region. The atmospheric circulation related to the SIC–precipitation anomalies was analysed using data from the NCEP/NCAR Reanalysis (Kalnay *et al.*, 1996) and includes monthly mean 850 and 700 hPa geopotential height (Z850 and Z700, respectively), specific humidity (q) and temperature (T) from 1000 to 700 hPa, precipitable water and zonal and meridional wind components (u and v , respectively) from 1000 to 250 hPa.

As all datasets considered in this article have at least partially been derived using remote sensing data, the period of analysis was selected so as to be included in the satellite era and runs from January 1981 to July 2008. Two distinct seasons were considered for analysis in terms of the seasonality of SIC around Antarctica, as done previously in Kidston *et al.* (2011): summer (January–February–March; JFM) and winter

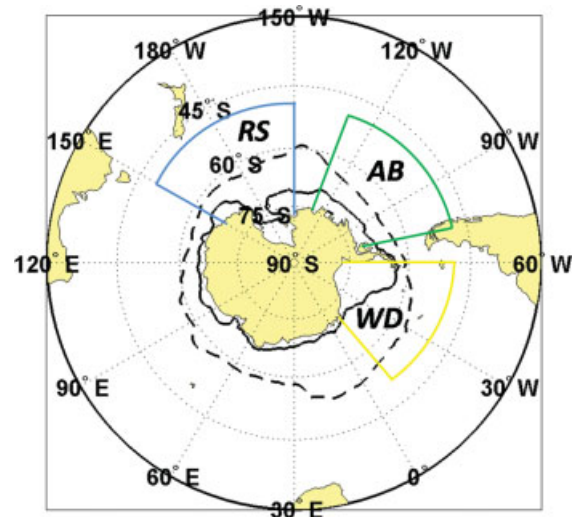


Figure 1. Mean SIE position in February (full black line) and September (dashed black line). The Ross, Amundsen–Bellingshausen and Weddell Sea regions are indicated by RS, AB and WD, respectively.

(August–September–October; ASO; which is truly late winter–early spring in the SH but for simplicity will be called winter). A total of 84 (=3 months \times 28 years) summer and 81 (=3 months \times 27 years) winter months were thus obtained.

The relationship between SIC and South America precipitation was analysed considering three high latitude areas separately: the Ross Sea (from 50°S to the Antarctic coast and from 150°E to 150°W), the Amundsen–Bellingshausen (from 50°S to the Antarctic coast and from 130°W to 70°W) and the Weddell Sea (from 50°S to the Antarctic coast and from 60°W to 10°W). The location of the three areas is shown in Figure 1. The mean SIE position was computed by taking for each longitude the latitude at which sea ice concentration was equal to 0.15 as done in previous works (Renwick, 2002). Accordingly, sea regions were classified as ‘ice covered’ whenever the sea ice concentration was equal to or above 0.15.

Anomalies of SIC and precipitation over South America were derived by subtracting to each month its corresponding long-term mean. Linear trends on the resulting time series were computed and removed afterwards. Correlation coefficients and their significance were then calculated between the detrended SIC and South American precipitation anomalies time series. To isolate the effect of known modes of SH atmospheric variability on SIC (Lefebvre and Goosse, 2008), linear regressions of SIC on the time series of SAM and ENSO indices were computed following Equations 1 and 2 and the resulting time series – with ENSO and SAM contributions removed – were used to recalculate the previous correlations. SAM and ENSO indices were obtained from the NCEP Climate Prediction Center (<http://www.cpc.ncep.noaa.gov/>).

$$\text{SIC}_{\text{filt}ij} = \text{SIC}_{ij} - \text{regr}_{ij} \quad (1)$$

$$\text{regr}_{ij} = a_{0ij} + a_{1ij} \cdot \text{SAM}_j + a_{2ij} \cdot \text{ENSO}_j \quad (2)$$

In Equations 1 and 2, SIC stands for the ‘full’ SIC time series (only with annual cycle and trend removed) and SIC_filt for that with no SAM and ENSO contributions. regr, the regressand or response function, was computed by using SAM and ENSO indices as predictors, and the regression coefficients (a_0 , a_1 and a_2) were obtained by least square fitting. i stands for the different regions (Amundsen–Bellingshausen Sea, Weddell Sea and Ross Sea) and j , for the two seasons, summer and winter.

SIC anomalies (both with and without SAM and ENSO contributions) were grouped for each region in high (low) cases considering months within a season in which SIC anomaly was above (below) the 80th (20th) percentile of the corresponding season. These months were then taken together to compute the related patterns of anomalous atmospheric circulation over the SH for the three regions, for summer and winter and for both high and low SIC cases.

To explain the observed anomalies in South American precipitation associated to the different SIC patterns, precipitable water and low-level moisture fluxes anomalies were calculated for high and low SIC cases. The low-level moisture flux Q is defined as:

$$Q = \frac{1}{g} \int_{P_1}^{P_0} qV \, dp \quad (3)$$

In Equation 3, g stands for gravity acceleration, q , the specific humidity and V , the horizontal wind vector. P_0 and P_1 stand for atmospheric pressure at 1000 and 700 hPa, respectively, where the largest portion of global moisture is concentrated.

Atmospheric perturbations that enhance lifting motion and contribute with the production of precipitation at midlatitudes are usually related to conditions of baroclinic instability (Hoskins and Valdes, 1990). Lindzen and Farrell (1980) showed that the Eady growth rate (σ) is a good measure of the magnitude of atmospheric baroclinic instability. This variable takes into account the low-level vertical shear and the static stability and is defined as:

$$\sigma = 0.31f \cdot \left| \frac{dV}{dz} \right| \cdot \left(\frac{g}{\theta} \frac{\partial \theta}{\partial z} \right)^{-1} \quad (4)$$

where f is the Coriolis parameter ($=2\Omega \cdot \sin\varphi$, being Ω the Earth’s angular velocity and φ the latitude), V the horizontal wind vector and θ , the potential temperature. Vertical variations were considered between 850 and 700 hPa. This variable is used in this paper to compute variations in the baroclinic instability (and resulting potential of atmospheric perturbation growth) at midlatitudes related to the different SIC scenarios.

Since Lemke *et al.* (1980) had already stated that SIC anomalies tend to persist for several consecutive months and are thus capable of altering the atmospheric and oceanic circulation, seasonal predictability of dry/wet conditions over South America using SIC as predictor is also assessed by computing lagged composites between

winter SIC anomalies over the Southern Ocean and spring rainfall anomalies on South America. As river discharges are mainly driven by precipitation and temperature, further analysis is performed to link anomalous sea ice patterns with selected river streamflow anomalies at the outlet of large basins. Streamflow data were obtained from the *Subsecretaría de Recursos Hídricos* (Undersecretary of Water Resources) of Argentina and the *Operador Nacional do Sistema Eléctrico* (National Electric System Operator) of Brazil and consist of monthly mean discharges of the Uruguay River at Paso de los Libres (29°43’S, 57°04’W), the Iguazú River at Salto Caxias (25°33’S, 53°30’W), the Paraná River at Jupia (20°47’S, 51°38’W) and Itaipú (25°25’S, 54°36’W) and the Sao Francisco River in Tres Marias (18°12’S, 45°14’W) and Lago de Itaparica (9°00’S, 38°20’W).

3. SIC and precipitation variability

3.1. Sea ice

Figure 1 shows the mean February and September location of the SIE, when sea ice reaches its minimum and maximum latitudinal extension respectively. During February SIC is rather small around the Southern Ocean except for the Weddell Sea region where much of the region remains ice covered. In September, however, the only region where SIC is scarce is west of the Antarctic Peninsula, but over the rest of the Antarctic coasts sea ice is found everywhere and in some places extending up to about 53°S, as is the case of the South Atlantic Ocean. Tables 1 and 2 show mean SIC over the Ross, Amundsen–Bellingshausen and Weddell regions during summer and winter. In both seasons the Weddell Sea has the largest SIC values, with more than $4.0 \times 10^6 \text{ km}^2$ (almost 60% of the region) ice covered during winter. The Amundsen–Bellingshausen Sea region is only 7% ice covered ($4.0 \times 10^5 \text{ km}^2$) during summer and 27% ($2.1 \times 10^6 \text{ km}^2$) in winter, while the Ross Sea area varies between 0.4 and $3.4 \times 10^6 \text{ km}^2$.

Figure 2 displays the time series of SIC percentage anomalies in the three regions during summer and winter respect to their corresponding long-term means. For summer, besides the positive trend in SIC over the Ross and Weddell Seas and the negative trend over the Amundsen–Bellingshausen region, time series exhibit large year-to-year variability and a changing relationship among them. For instance, although in the beginning of the analysis period there appeared to be a positive correlation between Ross and Amundsen–Bellingshausen SIC, from about 1998 onward this relationship seems to have reversed in sign. Table 1 includes information on linear trends and correlation coefficients and their significance computed between the three SIC time series. These results indicate the strongest link is found between the Ross and the Weddell regions, with $r \approx 0.5$, significant at the 99% confidence level after a t -test. Though significant, the link between the Ross and the Amundsen–Bellingshausen area is much weaker.

Table 1. Mean area covered in sea ice (in km²) and its trend (in km² per decade) in the Ross, Amundsen–Bellingshausen and Weddell Sea regions in summer, and correlation coefficients between the three time series.

Region	SIC (10 ⁶ km ²)	SIC trend (10 ⁴ km ² decade ⁻¹)	R _{Ross}	R _{Amundsen}	R _{Weddell}
Ross	0.42	0.00	1.000	0.191*	0.494**
Amundsen	0.40	−0.16*	0.191*	1.000	0.125
Weddell	1.48	1.04*	0.494**	0.125	1.000

Significance at 90% and 99% confidence levels are marked with * and **, respectively.

Table 2. Mean area covered in sea ice (in km²) and its trend (in km² per decade) in the Ross, Amundsen–Bellingshausen and Weddell Sea regions in winter, and correlation coefficients between the three time series.

Region	SIC (10 ⁶ km ²)	SIC trend (10 ⁴ km ² decade ⁻¹)	R _{Ross}	R _{Amundsen}	R _{Weddell}
Ross	3.40	0.70	1.000	−0.155	0.046
Amundsen	2.10	0.09	−0.155	1.000	−0.114
Weddell	4.05	−0.37	0.046	−0.114	1.000

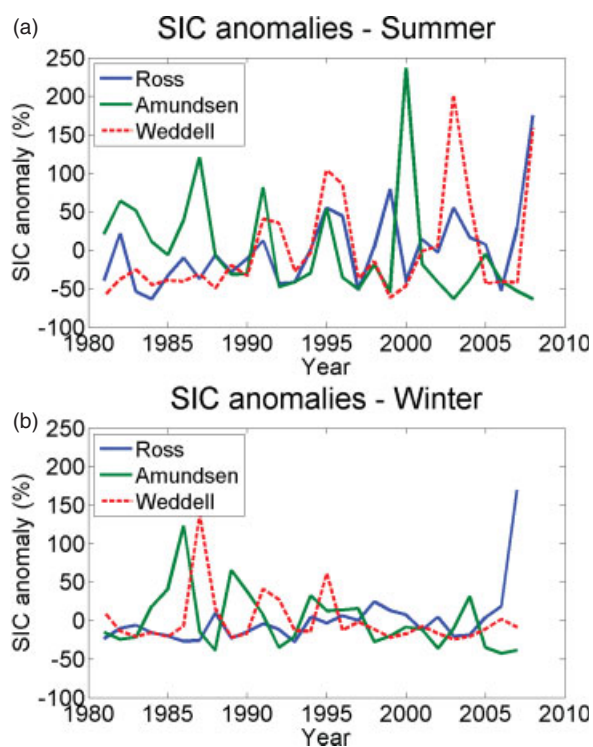


Figure 2. Sea ice cover (SIC) percentage anomalies in (a) summer, and (b) winter in the Ross, Amundsen–Bellingshausen and Weddell regions respect to the corresponding 1981–2008 mean.

Linear trend analysis indicates increases in SIC over both the Ross and Weddell Seas and receding ice cover over the Amundsen–Bellingshausen region which could be related to the large positive temperature trends registered there (Monaghan *et al.*, 2008). An analysis of the statistical significance of the trends using the nonparametric Mann–Kendall test (Mann 1945, Kendall 1955) indicates the only significant trends are those of the Amundsen–Bellingshausen Sea (negative) and Weddell Sea (positive), both in summer. These trends in SIC are consistent with previous findings by other authors using longer periods of analysis (Liu *et al.*, 2004).

In winter, interannual SIC variability is reduced compared to summer. In fact, in this season there are only 3 years when SIC exceeded +100% anomaly with respect to its mean in any region, compared to the six occurrences found in summer. The most extreme month of any region occurred in 2007 over the Ross Sea area, with a SIC anomaly surpassing +150% above the mean values for the cold season. Although not being the scope of this paper, it is worth mentioning that this case could be linked to the extremely cold conditions registered during that winter over much of central and southern South America. Linear trends on the three time series (Table 2) indicate upward SIC trends only over the Ross Sea region, with an increase of about 22% per decade, and negative trends over both the Amundsen–Bellingshausen (−15.9% per decade) and Weddell (−8.9% per decade) regions. Annually, SIC increased during this period over the Ross and Amundsen–Bellingshausen Seas and decreased in the Weddell Sea (not shown).

3.2. Precipitation

Rainfall over much of central and northern South America has a well defined seasonal pattern, with rainy conditions from October to March and prevailing dry conditions during the rest of the year. Figure 3 shows the precipitation climatology for summer and winter as defined in this article. Summer accounts for much of the total annual rainfall in a large portion of the region, especially from the equator to about 20°S where winters are very dry. Over SESA, however, there is a relative maximum near the Atlantic coast of nearly 4 mm day⁻¹ during the cold season. In this season there is also a precipitation maximum west of the Andes Mountains south of 30°S. Interannual standard deviation values maximize during summer over tropical South America (about 3 mm day⁻¹) and in the rest of the year over SESA. However, there is a relative standard deviation maximum over tropical South America centered in about 10°S during winter which is partially related to the fact that the definition

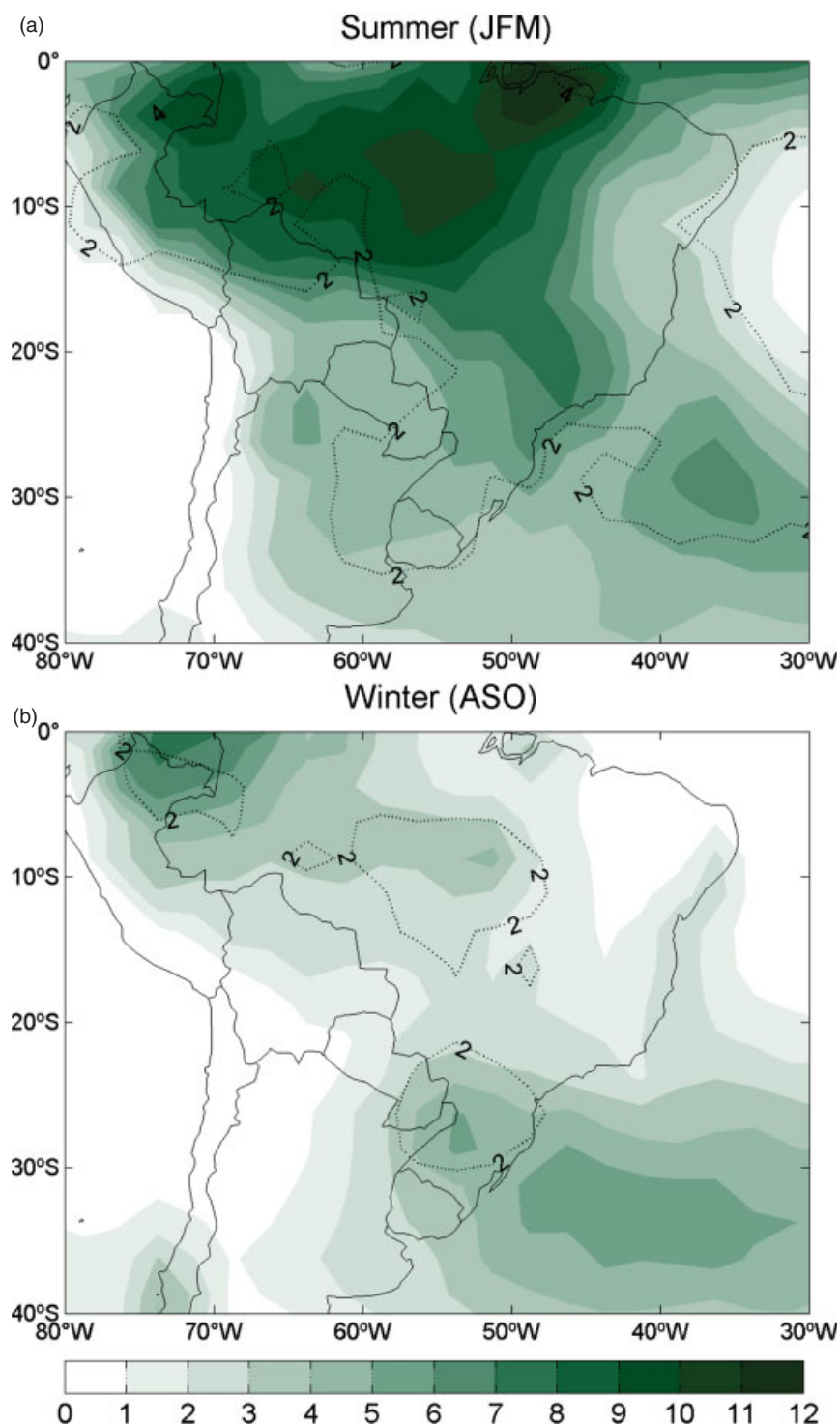


Figure 3. Precipitation mean (shaded) and interannual standard deviation (contours) over South America in (a) summer (JFM), and (b) winter (ASO). Units are mm day⁻¹.

of winter considered in this article – following SIC seasonality – includes the early stages of the rainy season over tropical South America (Marengo *et al.*, 2001).

3.3. SIC-precipitation covariability

Figure 4 shows the correlation coefficient between detrended and annual cycle removed Ross, Amundsen–Bellingshausen and Weddell SIC and precipitation in

South America in both summer and winter. During summer, the most outstanding feature is that SIC anomalies over any of the three regions are positively (and significantly) correlated with precipitation over eastern Brazil, particularly over the South Atlantic Convergence Zone (SACZ; Kodama, 1992). The largest signal there appears related to the Weddell Sea region. Further south, over Uruguay and northeastern Argentina there are hints

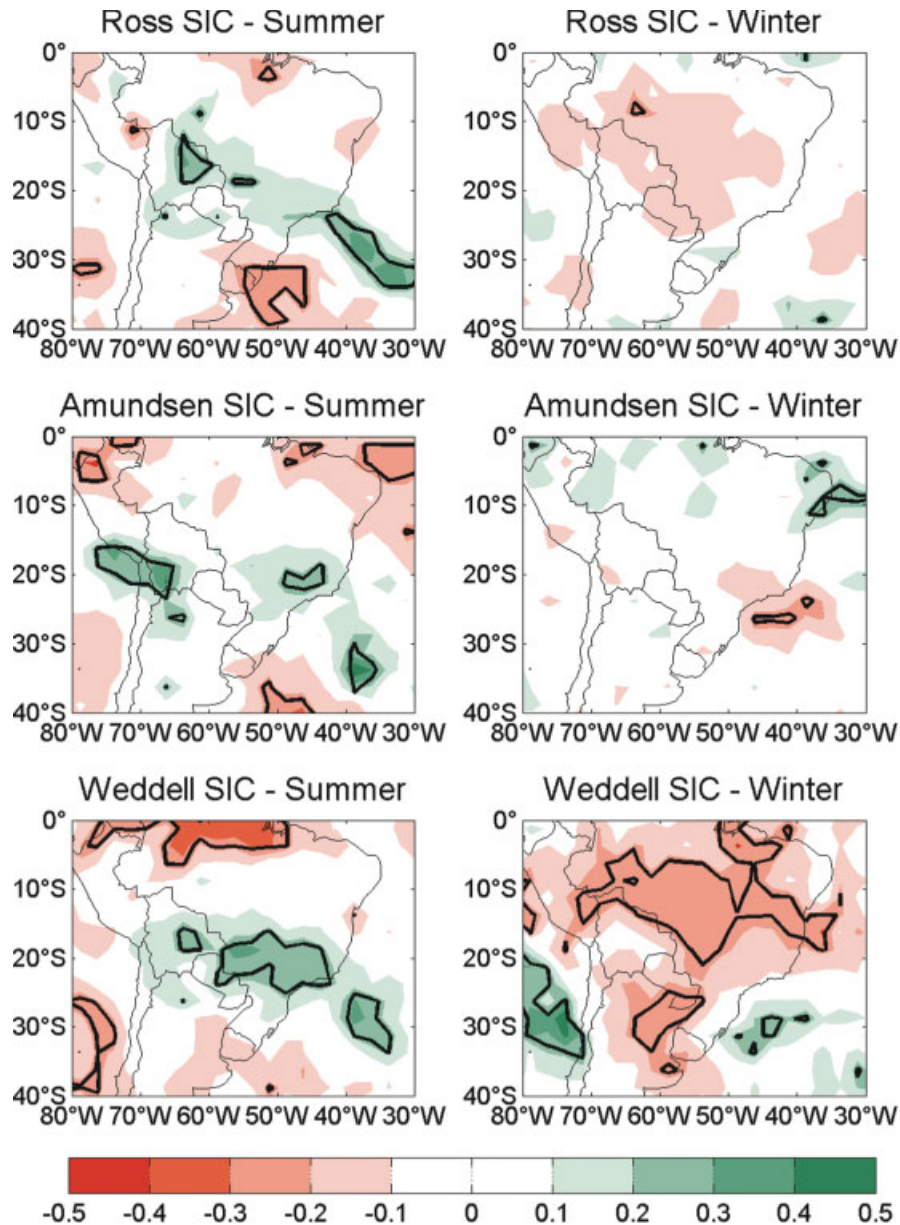


Figure 4. Correlation coefficients between deannualized, detrended Ross (top), Amundsen–Bellingshausen (middle) and Weddell (bottom) SIC and South American precipitation in summer (left) and winter (right). The thick black line indicates regions where correlation is significant at the 5% confidence level following a *t*-test.

of a negative correlation which may actually be related to the dipolar pattern of precipitation between this region and the SACZ area (Nogués-Paegle and Mo, 1997) but significance is low there. The exceptions to this are SIC anomalies in the Ross Sea area, which are negatively and significantly correlated with Uruguay and southern Brazil summer precipitation. The northern edge of South America, near the equator, also tends to have an opposite pattern of variability to that of sea ice over the Southern Ocean, and although the scope of the article is constrained to the influence of the sea ice extent on precipitation over SESA, the noticeably sea ice-related anomaly in precipitation over equatorial South America during summer deserves a comment. As expected from

an extension to the north of the sea ice on the Weddell region, the middle and upper troposphere circulation and its westerly maximum displace equatorward as well, leaving the jet about 40–45°S and its intermittent subtropical branch reaching lower latitudes more frequently. Therefore, more anticyclonic conditions prevail south of the SACZ resulting in less frequent low-level jet events east of the Andes, which are normally responsible for a substantial part of the moisture transport towards subtropical latitudes. This favours the enhancement of the positive SACZ phase (Nogués-Paegle and Mo, 1997, Doyle and Barros, 2002) with consequently increased moisture transport from the equatorial region (Figure 9(a)). In addition, the enhanced convection over the SACZ is

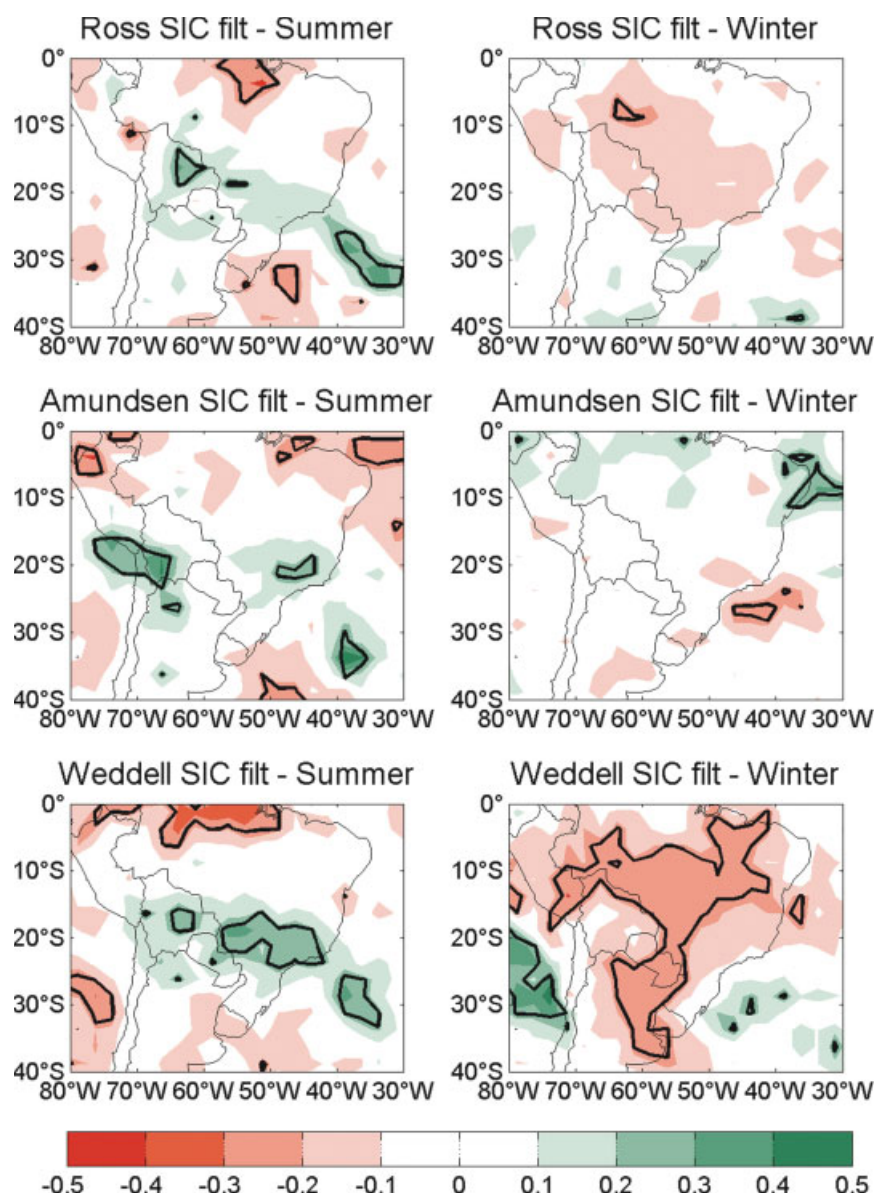


Figure 5. Correlation coefficients between deannualized, detrended Ross (top), Amundsen–Bellingshausen (middle) and Weddell (bottom) after filtering out but after filtering out the effects of SAM and ENSO from the SIC time series. The thick black line indicates regions where correlation is significant at the 5% confidence level following a *t*-test.

accompanied by increased moisture convergence and precipitation over eastern-southeastern Brazil and divergence at low levels in the equatorial region (see the increase in vector size from the equator towards 10–15°S over northern Brazil in Figure 9) leading to less precipitation there.

In the cold season not much impact on precipitation is seen associated to SIC anomalies over the Ross and Amundsen–Bellingshausen areas, but a distinct pattern is related to ice on the Weddell Sea region. In fact, SIC is negatively and significantly correlated with precipitation over much of central and northern South America and positively correlated with rainfall west of the Andes, affecting a portion of central Chile and the Andes Mountains near 30–35°S. Winter is the rainy season there, and this suggests enhanced precipitation activity

in years with increased SIC in the Weddell region. In particular over the Amazon region, where negative correlations are found, this behavior could be related to a delay in the onset of the South American Monsoon activity (Vera *et al.*, 2006), potentially prolonging the length of the dry season. This will be further analysed in the section related to seasonal predictability.

Table 3 lists the correlation coefficients between SAM and ENSO indices and deannualized, detrended SIC time series on the three regions. No correlation is above 0.3 and statistical significance is only achieved in the case of SAM in summer with the Ross and Amundsen–Bellingshausen SIC and during winter between ENSO and the Ross and Weddell SIC. Figure 5 displays linear correlation coefficients between SIC and

Table 3. Correlation coefficients between SIC in the three regions and the SAM and ENSO indices for summer and winter.

	Summer		Winter	
	SAM	SOI	SAM	SOI
Ross	0.211*	−0.103	−0.136	−0.268**
Amundsen	0.181*	−0.051	0.145	0.133
Weddell	0.010	0.131	−0.032	0.229**

* and ** indicate correlations that are statistically significant at 90% and 95% confidence levels.

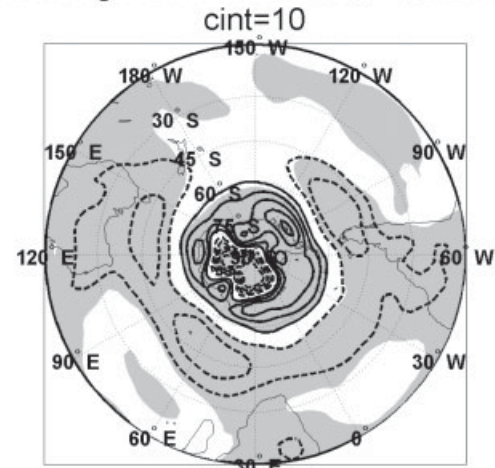
precipitation, as in Figure 4, but computed after removing ENSO and SAM trends from the SIC time series (Equation 1). As it can be seen, patterns are very much the same to those shown in Figure 4 for both seasons and the three SIC regions. In fact in some regions correlation increases and becomes thus more strongly significant, as is the case of much of central and northern Argentina in winter related to SIC in the Weddell Sea region. Given that the relationship between SIC and precipitation variability is largest for the Weddell region, the rest of this article will focus on that area in particular.

4. Atmospheric circulation related to SIC variability

Many studies have shown that SIC is not independent of atmospheric circulation. For instance, meridional thermal advection is one of the primary mechanisms to explain the progression and recession of sea ice (Dash *et al.*, 2012). Figure 6 shows the Z850 anomaly composites considering the difference between high minus low SIC cases in the Weddell Sea region for summer and winter – with ENSO and SAM effects on sea ice removed. SIC anomalies during summer are associated to a dipolar pressure pattern (very similar to the SAM), with high values over the coasts of Antarctica and low pressures anomalies over southern South America, the southern Indian Ocean and southeastern Australia. In winter, however, there are weak positive height anomalies on southern South America, leading to drier conditions over southern Chile (Figure 5). Likewise, negative pressure anomalies are present over the South Indian Ocean. Anomalies related to both the dipolar summer pattern described previously and those associated to high pressure over southern South America and low pressure over the South Indian Ocean in winter are significant at the 99% level according to a *t*-test.

Figures 7 and 8 show summer and winter mean zonal wind at 250 hPa (u_{250}), 500 hPa-circulation and σ along with the observed differences in high minus low SIC cases in the Weddell Sea. It is important to note that although σ is largely determined by the intensity of upper level winds and thus attains maximum values at mid-latitudes in the cold season when winds are strongest, σ anomalies as considered in this study are independent of the seasonality and can thus give hints of the baroclinic forcing acting on particular SIC

(a) h850 high-low Weddell SIC - Summer



(b) h850 high-low Weddell SIC - Winter

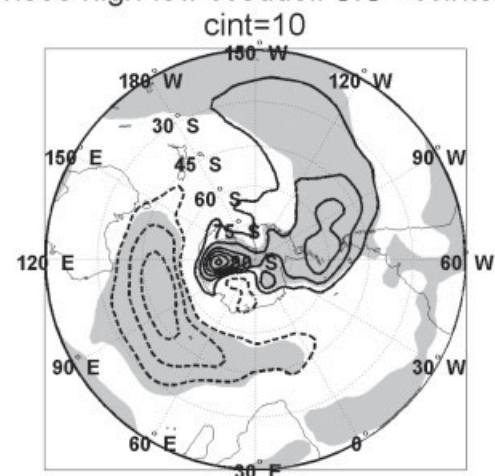


Figure 6. 850 hPa-Geopotential height anomalies composite of high minus low cases [i.e. months when SIC was above (below) the 80th (20th) percentile, respectively] for the Weddell Sea region in (a) summer, and (b) winter. Units are $\text{m}^2 \text{s}^{-2}$. Contour interval (*cint*) is $10 \text{ m}^2 \text{s}^{-2}$ with zero contour omitted. Shaded areas are significant at the 99% level.

conditions. During summer (Figure 7), the upper level jet on South America has a maximum around 50°S with mean velocities of about 35 m s^{-1} over the South Atlantic Ocean. Two troughs are present in the mean 500 hPa wind field around South America: one centered in 75°W near the coast of Chile (from now on, LOW-W), and another one in 50°W , east of SESA (LOW-E). Eady growth rate has a maximum located over southern South America of about $8 \times 10^6 \text{ s}^{-1}$.

The composite of high minus low SIC cases in the Weddell Sea is characterized by a stronger upper level jet over southern South America with a maximum difference near 40°S . Negative zonal wind differences are found further north suggesting a northward displacement of the jet with increased ice in the Weddell. Weaker zonal winds are also found at 60°S , suggesting that maximum westerlies are displaced northward when sea ice is increased in the Weddell region. This pattern of equatorward displacement of the polar jet is also

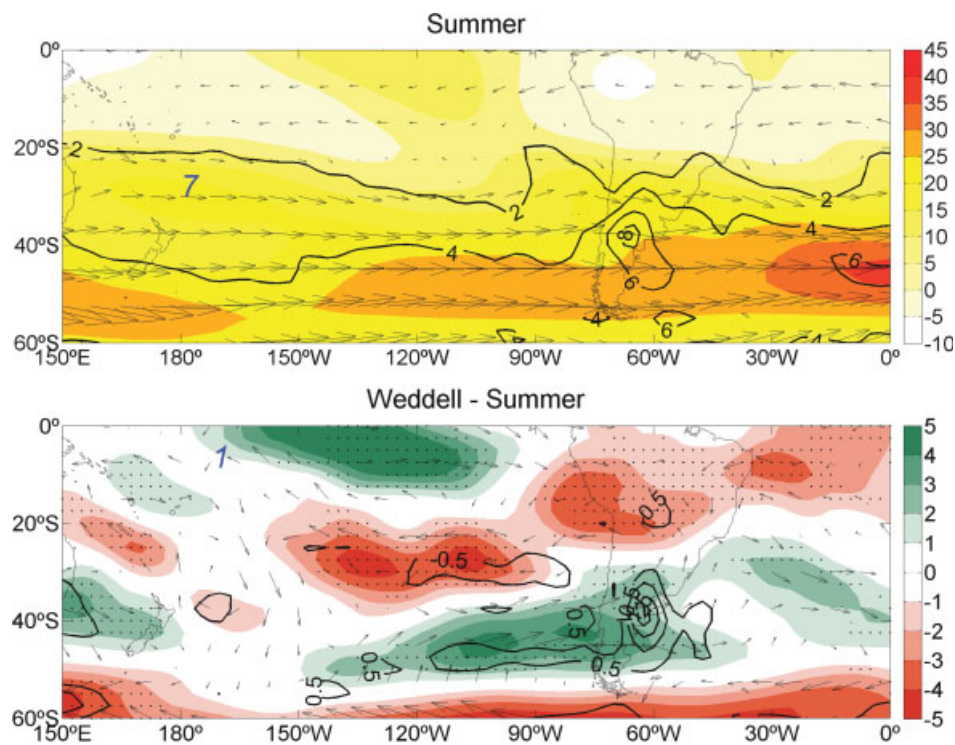


Figure 7. Mean 250hPa-zonal wind u (shaded; m s^{-1}), mean 500 hPa circulation (vectors) and Eady growth rate (contours; $\times 10^6 \text{ s}^{-1}$) in summer (top). High minus low Weddell SIC departures from the corresponding mean values (bottom). Numbers in blue in both panels denote the magnitude of the closest 500 hPa wind vector (m s^{-1}) for reference. Black dots in the bottom figure depict significance of u anomalies at the 99% level.

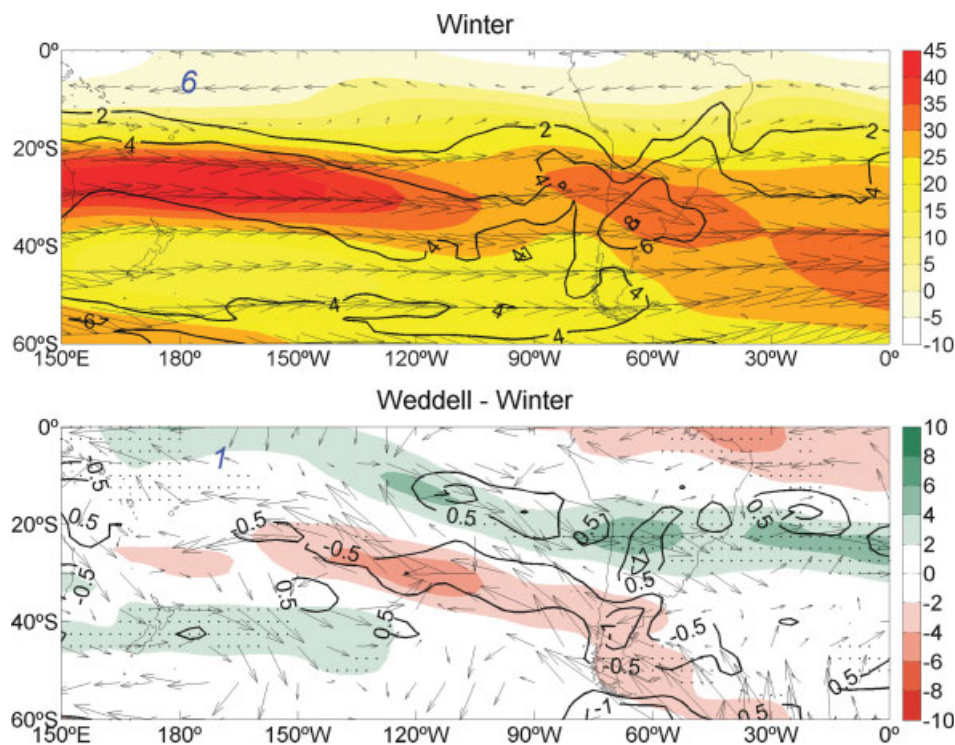


Figure 8. Mean 250hPa-zonal wind u (shaded; m s^{-1}), mean 500 hPa circulation (vectors) and Eady growth rate (contours; $\times 10^6 \text{ s}^{-1}$) in winter (top). High minus low Weddell SIC departures from the corresponding mean values (bottom). Numbers in blue in both panels denote the magnitude of the closest 500 hPa wind vector (m s^{-1}) for reference. Black dots in the bottom figure depict significance of u anomalies at the 99% level. Note that the wind speed colour bar in the bottom panel differs from that of Figure 7.

found when SIC anomalies over the other regions are considered (not shown). In the 500 hPa circulation, the LOW-E favours upward motion over the SACZ region. The LOW-W tends to be reduced and shifted southwest of its mean position. Eady growth rate is increased over southern South America near 40°S, partly related to the enhanced upper level winds and vertical wind shear, and also over subtropical South America at about 20°S which is linked to the rainier conditions during summer in that region.

In winter (Figure 8), stronger upper level winds are seen over South America with a mean value in excess of 40 m s⁻¹ in the South Pacific. Only one trough is found in the regional 500 hPa wind field near southern South America, now centered over the Andes Mountains and leaving much of SESA in the region prone to upward motion that, however, is not related to an increase in precipitation due to the low precipitable water as it will be shown later. σ values depict once again a maximum over southern South America but their magnitudes are smaller than during the warm season, probably related to the colder, more stable low-level conditions prevailing in winter. Yet, a positive anomaly is found reaching the coast of central and northern Chile, partly explaining the winter rainfall in that region and its relation to the SIC anomalies in the Weddell Sea. Positive SIC differences over the Weddell region are associated to an extended positive anomaly in u250 over the Pacific Ocean in about 40–45°S, with negative differences to the north. Conditions over South America are characterized by more intense winds in subtropical latitudes (around 25–30°S) and weaker zonal winds to the north and south. It is interesting to see that the 500 hPa circulation difference is characterized by a ridge axis over northern Chile and Argentina, centered near 20°S, 60°W, which enhances sinking motion over northern Argentina, Uruguay and southern Brazil, while a trough downstream of that ridge leads to an increase in lifting motion over the South Atlantic (not shown). Northern South America is characterized by 500 hPa wind anomalies from the east.

Moisture flux and precipitable water composites of the difference between high minus low SIC cases in the Weddell Sea for summer and winter are shown in Figure 9. During summer, moisture fluxes from the north are enhanced over northern South America but in about 15°–20°S they are deflected towards the east, converging further east in the climatological SACZ position. As moisture fluxes are deflected eastwards the SACZ becomes more active, but at the same time less moisture is transported southwards onto southern South America. Active SACZ seasons are known to be related to drier conditions over northern Argentina/Uruguay as low level jet events (which explain a large part of the warm season precipitation over these areas) become less frequent (Doyle and Barros, 2002; Marengo *et al.*, 2004). Although all the analysis in this article is done on a monthly basis, this could suggest less daily frequency of northerly winds reaching northern Argentina with the resulting less fuel for convection. Again, strong SACZ are

usually related to more precipitation over west and central Argentina (Doyle and Barros, 2002) which is also seen in this pattern of moisture transport and precipitable water. In this case, however, this does not result in more precipitation because of the weakening of the trough over Chile.

When the cold season is analysed, a large and significant area of drier conditions/less precipitable water is seen over much of central and southern South America, covering from central Argentina to central-northern Brazil with large differences in the moisture fluxes from central South America northwards, onto the equatorial region of the continent. This leads to enhanced lift over northeast Brazil (not shown) with more precipitation there (Figure 5). Over central Chile lift is increased (not shown) and there is also a slight increase in moisture fluxes coming from the northwest that favour strong winter precipitation over the Andes Mountains (Viale and Núñez, 2011).

5. Seasonal precipitation and river discharges predictability

To analyse potential seasonal predictability on South American precipitation associated to SIC, lagged composites between both time series were computed. Figure 10 shows October and November mean precipitation over tropical and subtropical South America. In October, three distinct maxima can be found on the continent: one over northeastern Argentina and the surrounding areas of Brazil and Paraguay with rain rates of about 6–7 mm day⁻¹, another one over the equatorial region near 75°W and a third region over central-northern Brazil with mean precipitation values near 8 mm day⁻¹. This last maximum is related to the convective activity associated to the South American Monsoon. A relative minimum on precipitation is found further east, over the SACZ region. During November this pattern changes as the convective activity reaches the coast and establishes a well-defined SACZ pattern centered in a northwest-southeast oriented axis from central Brazil onto the Atlantic. The maximum located over northeastern Argentina still persists but its magnitude is reduced with respect to the previous month.

Figure 11 shows composites of precipitable water and Z850 anomalies in October and November associated to high minus low SIC cases on the Weddell region in September (i.e. one and two months preceding the precipitation anomalies patterns). In October (top panel) a large anticyclonic anomaly is found over the Weddell Sea region, centered near 70°S, while a cyclonic anomaly is present over SESA. This circulation anomaly is associated to higher precipitable water values on the coast of eastern and northern Brazil and drier conditions over much of northern Argentina and Uruguay – significant at the 99% confidence level following a *t*-test – which is very similar to that associated to cold ENSO (i.e. La Niña) events. Given that ENSO forcing has been removed, this result could indicate the presence of a

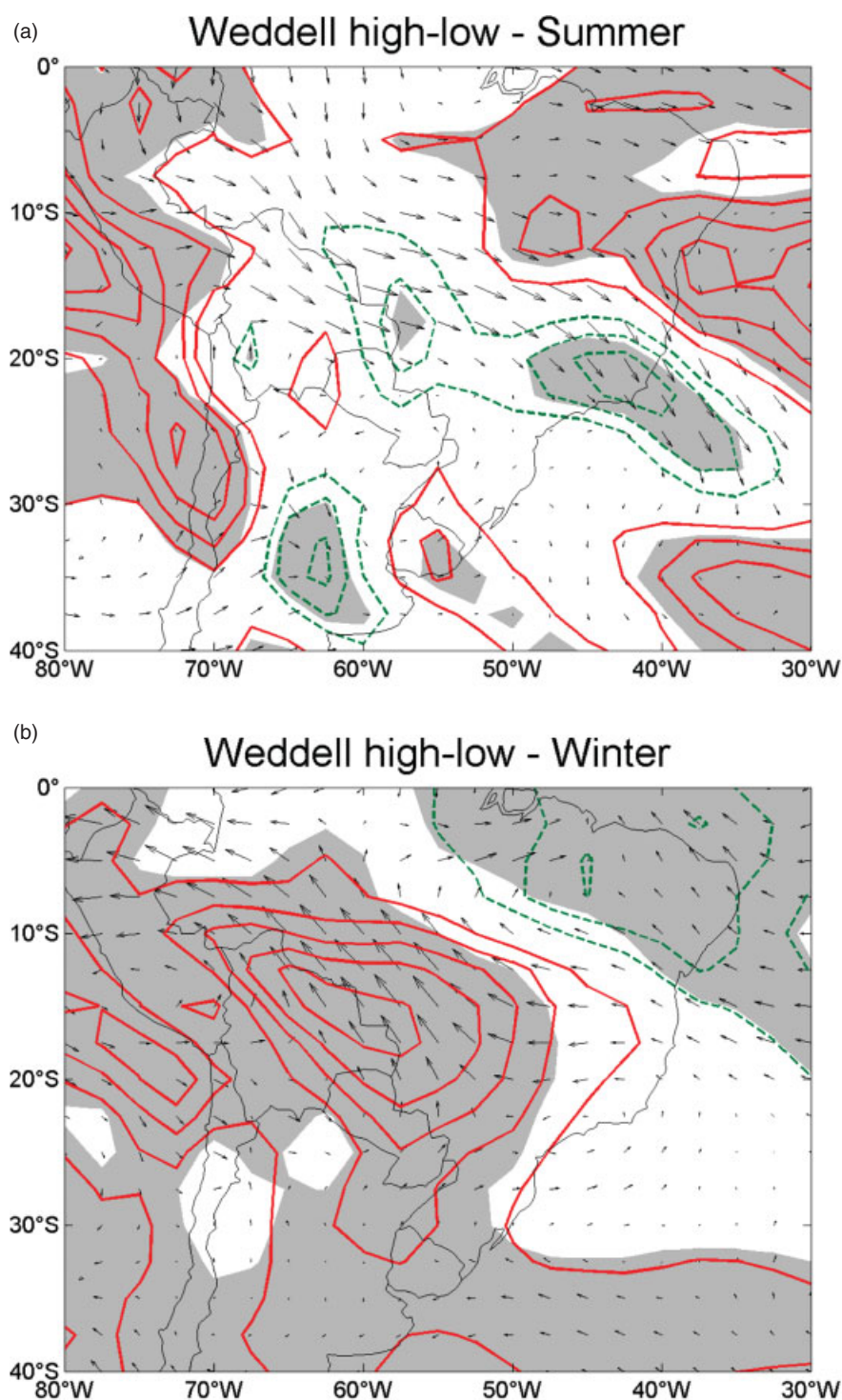


Figure 9. Moisture fluxes and precipitable water composites in high minus low SIC cases (see text for details) in the Weddell region in (a) summer, and (b) winter. Precipitable water units are mm and contour interval is 0.5 mm, with positive and negative values in dashed and full lines, respectively. Areas shaded in grey denote regions where precipitable water differences are significant at the 99% confidence level according to a *t*-test.

particular oceanic-atmosphere feedback related to these SIC anomalies acting even in the absence of ENSO. In November (bottom panel) the blocking pattern tends to persist, although the anticyclonic difference is now found further north and the Weddell region is instead located east of a cyclonic difference which enhances northerly winds over that area. The low pressure difference on

SESA persists and precipitable water anomalies are intensified respect to the previous month, with dry conditions in northern Argentina and Uruguay and wetter conditions to the north.

Figure 12 shows precipitation difference composites associated to the circulation differences of Figure 11. In October the pattern shows negative rainfall anomalies

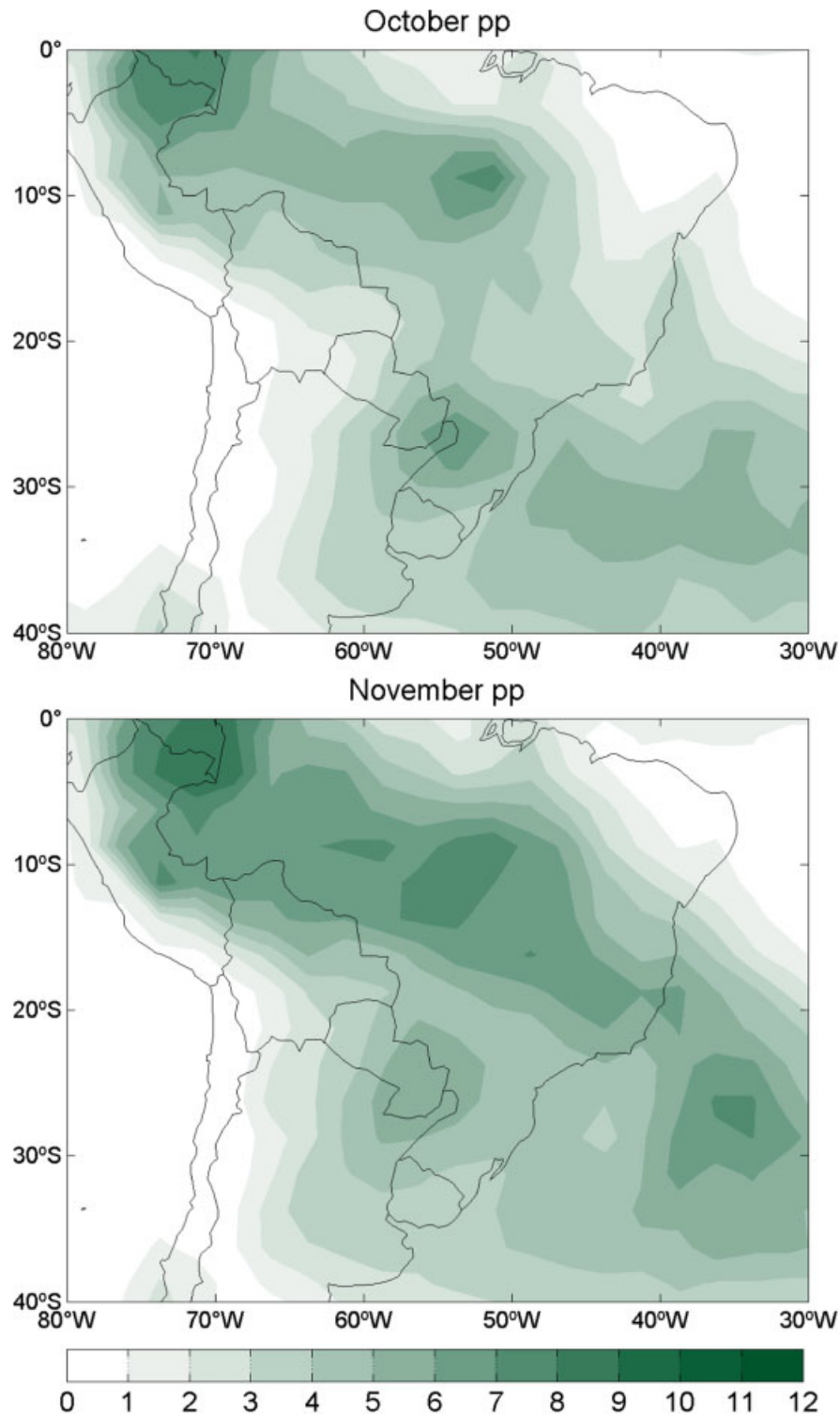


Figure 10. October (top) and November (bottom) mean precipitation in South America. Units are mm day⁻¹.

over southern Brazil and along the Peruvian-Brazilian border, both statistically significant according to the Student's t -test with a confidence level exceeding 99% (see black thick lines in Figure 12), while positive precipitation anomalies are seen over the SACZ region. In November the dry anomaly over northeastern Argentina not only persists, but is even more extended and intense

while the regions of central Brazil and the SACZ now are all associated to positive rainfall differences. A dry difference is further to the northwest, over the forest region of northern Peru and southern Colombia. In this month, both the dry anomaly over northeastern Argentina and the wet anomaly over central-eastern Brazil are significant at a 99% level.

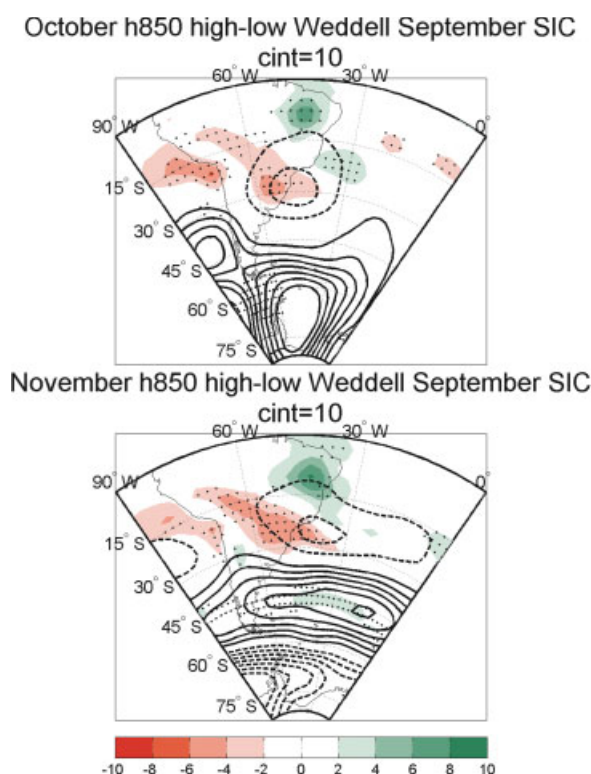


Figure 11. October (top) and November (bottom) precipitable water (shaded, in mm) and 850 hPa geopotential heights (contours, in $\text{m}^2 \text{s}^{-2}$) difference composites of high minus low cases in Weddell SIC in the preceding September. Black dots depict significance of precipitable water anomalies at the 99% level.

Since the location and persistence of the largest precipitation anomalies located in southern and central-eastern South America can exert a strong influence on river streamflow variability in the region, the Uruguay, Paraná, Iguazú and Sao Francisco basins were considered to assess the link between SIC-related rainfall anomalies and discharge variability (see discharge gauge locations in Figure 12). As for the SIC and rainfall time series, SAM and ENSO effects were also removed from discharge data through a linear regression analysis.

Considering the previous lagged SIC-rainfall analysis, Tables 4 and 5 include statistics of streamflow changes during the months of October and November, respectively, associated to SIC variability over the Weddell Sea region in the previous September. As streamflow data tend not to follow a Gaussian distribution, medians (and not means) are presented for October and November along with the differences in high and low SIC conditions in September. Overall, during October (Table 4) the Uruguay and Iguazú Rivers have their streamflow diminished when SIC in the Weddell is above the 80% percentile in September. For the gauging stations in the Paraná and Sao Francisco Rivers the patterns of streamflow anomalies are opposite to that of the Uruguay River, with positive (negative) anomalies related to positive (negative) September SIC anomalies. Linear correlation coefficients computed between these series and SIC variability including only extreme cases of sea ice are non

significant for all basins, with a sign reversal between the Uruguay-Iguazú Rivers and the Paraná River, closely following the dipolar precipitation anomaly pattern seen in Figure 12. For November (Table 5), discharge anomalies become larger in absolute value on the Uruguay basin. On the Paraná River, the anomaly pattern is similar to that of the previous month while over the Iguazú River conditions resemble those of the Uruguay basin. It is interesting to note that the correlation coefficients between November streamflow anomalies and SIC considering only the extreme cases are now significant at the 95% level over the Uruguay and Iguazú basins. In the case of the Sao Francisco River, the pattern is opposite: as correlation fields suggest enhanced (decreased) precipitation with positive (negative) SIC anomalies on the Weddell region, both October and November streamflow are above (below) average when SIC anomalies are positive (negative). In particular during November, anomalies are larger but not significant. The SIC signal is particularly noticeable in the Uruguay River basin, where the largest precipitation anomalies are located, but it is observed in the rest of the eastern South American basins as well.

6. Conclusions

This article showed that SIC variability in the Southern Ocean in the absence of ENSO and SAM effects can exert significant alterations on precipitation over SESA. In particular the Weddell Sea region was found to be the most correlated with precipitation differences over SESA in both summer (JFM) and winter (ASO). During the warm season, high SIC in the Weddell area is related to high pressure anomalies over the Antarctic coast and a low pressure anomaly over the southeastern Pacific Ocean, affecting the southern coast of Chile. Another cyclonic centre intensifies east of South America, contributing to more precipitation over the SACZ region. This is also related to drier conditions over northeastern Argentina. Moisture fluxes analysis revealed that these conditions are associated to an enhancement (weakening) of moisture transport towards the SACZ (northeastern Argentina), suggesting less frequency of low-level jet events.

In winter, high SIC conditions are associated to high pressure covering much of southern South America and the Antarctic Peninsula, with a ridge axis at mid-levels over northern Chile which leaves central and northern Argentina in a region prone to subsidence, and explains the drier conditions found there. Downstream of the aforementioned ridge, a trough axis leads to more precipitation over the Atlantic Ocean east of SESA. In terms of precipitable water, high SIC anomalies over the Weddell were found to be linked to drier (moister) conditions in central and southern (northeastern) South America. This suggests that positive SIC anomalies over the Weddell lead to a delay in the onset of the convective activity associated to the South American

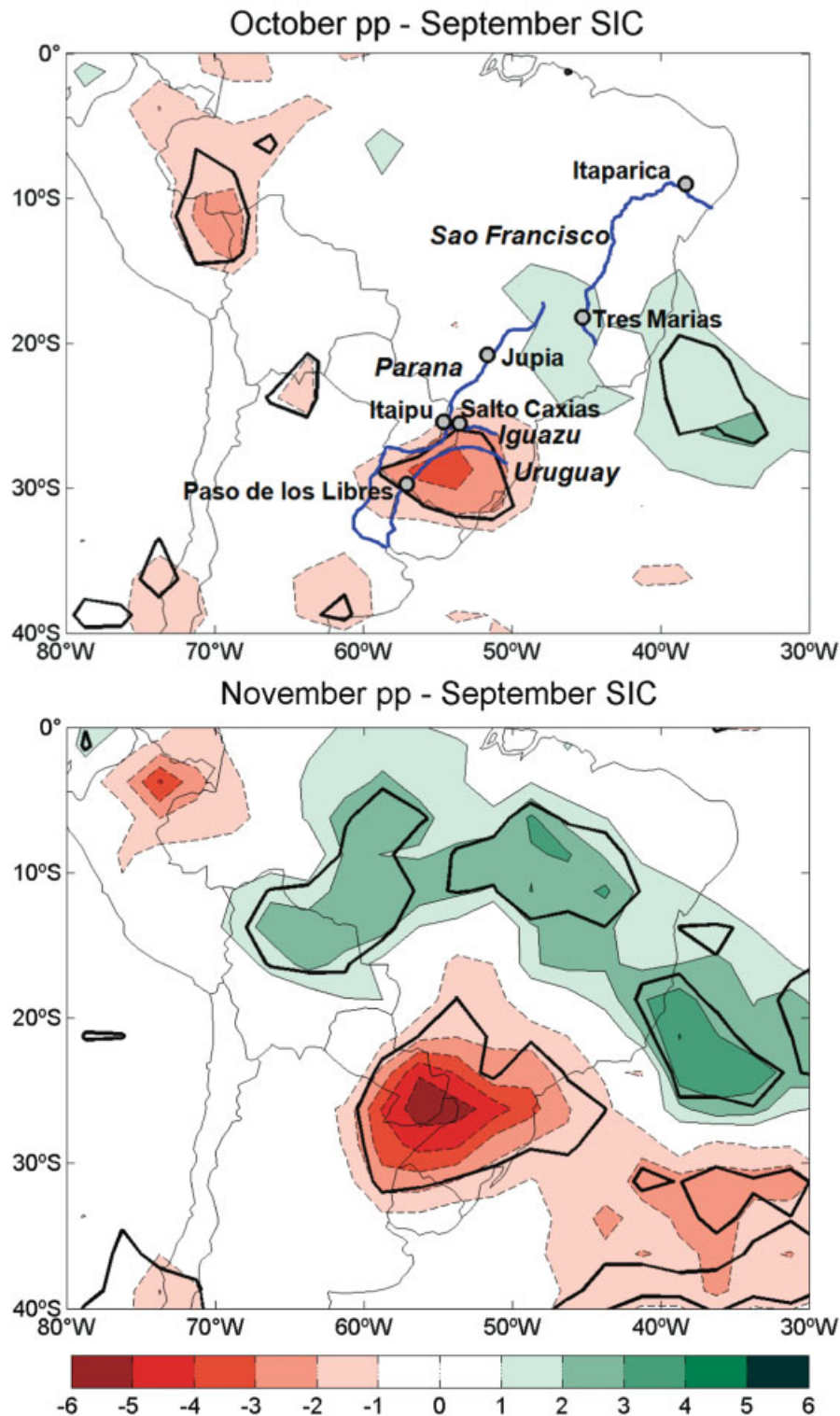


Figure 12. October (top) and November (bottom) mean precipitation difference composites of high minus low cases in Weddell SIC in the preceding September. Units are mm day^{-1} . The top panel also shows the locations of rivers (in italic) and discharge gauge locations. The black thick lines denote regions where precipitation differences are significant at the 99% confidence level.

Monsoon over central South America particularly around September–October.

SIC anomalies over the Weddell Sea during the peak of sea ice extension in the SH (i.e. September) are predictors of significantly drier (moister) conditions over northeastern Argentina and Uruguay (eastern

Brazil). High SIC cases in September are associated to a cyclonic anomaly over SESA which persists during the following two months and determines a distinct pattern of reduced (enhanced) precipitation over northeastern Argentina (eastern Brazil). These anomalies alter the river discharges of some basins across eastern South America,

Table 4. October median streamflow at selected gauging stations (first column), and anomalies in months when the previous September had extreme SIC in the Weddell region (second and third columns) with effects of ENSO and SAM removed from all time series.

	Q median ($\text{m}^3 \text{s}^{-1}$)	Q mean absolute difference in high SIC ($\text{m}^3 \text{s}^{-1}$)	Q mean absolute difference in low SIC ($\text{m}^3 \text{s}^{-1}$)	r (p -Value)
Paso de los Libres (Uruguay River)	6864	−2343	413	−0.33 (0.32)
Salto Caxias (Iguazu River)	1979	−855	464	−0.36 (0.27)
Jupia (Parana River)	4064	161	−528	0.26 (0.43)
Itaipu (Parana River)	8585	720	−1047	0.17 (0.62)
Tres Marias (Sao Francisco River)	245	31	−43	0.17 (0.61)
Itaparica (Sao Francisco River)	964	103	−66	0.15 (0.67)

Table 5. November median streamflow at selected gauging stations (first column), and anomalies in months when the previous September had extreme SIC in the Weddell region (second and third columns) with effects of ENSO and SAM removed from all time series.

	Q median ($\text{m}^3 \text{s}^{-1}$)	Q mean absolute difference in high SIC ($\text{m}^3 \text{s}^{-1}$)	Q mean absolute difference in low SIC ($\text{m}^3 \text{s}^{-1}$)	r (p -Value)
Paso de los Libres (Uruguay River)	4372	−2185	5178	−0.62 (0.04)
Salto Caxias (Iguazu River)	1430	−358	1273	−0.63 (0.04)
Jupia (Parana River)	4744	421	−258	0.13 (0.70)
Itaipu (Parana River)	8767	−264	984	−0.14 (0.68)
Tres Marias (Sao Francisco River)	442	0	−91	0.26 (0.44)
Itaparica (Sao Francisco River)	1590	112	−590	0.38 (0.25)

and consequently they can be used as a seasonal prediction tool for river management.

Acknowledgements

This research was supported by the University of Buenos Aires UBACYT- 20020100100803, Consejo Nacional de Investigaciones Científicas y Técnicas PIP2009-00444 and Agencia Nacional de Promoción Científica y Tecnológica PICT07-00400. Thanks to two anonymous reviewers for their comments that helped improve this article.

References

- Brayshaw DJ, Hoskins B, Blackburn M. 2008. The storm-track response to idealized SST perturbations in an aquaplanet GCM. *J. Atmos. Sci.* **65**: 2842–2860.
- Cai W, Whetton PH, Karoly DJ. 2003. The response of the Antarctic Oscillation to increasing and stabilized atmospheric CO_2 . *J. Climate* **16**: 1525–1538.
- Dash MK, Pandey PC, Vyas NK, Turner J. 2012. Variability in the ENSO-induced southern hemispheric circulation and Antarctic sea ice extent. *Int. J. Climatol.* **33**(3): 778–783, DOI: 10.1002/joc.3456.
- Deser C, Walsh JE, Timlin MS. 2000. Arctic sea ice variability in the context of recent atmospheric circulation trends. *J. Climate* **13**: 617–633.
- Doyle ME, Barros VR. 2002. Midsummer low-level circulation and precipitation in subtropical South America and related sea surface temperature anomalies in the South Atlantic. *J. Climate* **15**: 3394–3410.
- Grimm AM, Barros VR, Doyle ME. 2000. Climate variability in southern South America associated with El Niño and La Niña events. *J. Climate* **13**: 35–58.
- Hoskins BJ, Valdes PJ. 1990. On the existence of storm-tracks. *J. Atmos. Sci.* **47**: 1854–1864.
- Justino F, Peltier W. 2006. Influence of present day and glacial surface conditions on the Antarctic Oscillation/Southern Annual Mode. *Geophys. Res. Lett.* **33**: L22702, 1–6, DOI: 10.1029/2006GL027001.
- Kalnay E, Kanamitsu M, Kistler R, Collins W, Deaven D, Gandin L, Iredell M, Sha S, White G, Woollen J, Zhu Y, Chelliah M, Ebisuzaki W, Higgins W, Janowiak J, Mo KC, Ropelewski C, Wang J, Leetmaa A, Reynolds R, Jenne R, Joseph D. 1996. The NCEP/NCAR 40-year reanalysis project. *Bull. Am. Meteorol. Soc.* **77**: 437–471.
- Kendall M. 1955. *Rank Correlation Methods*, 5th edn., M Kendall and J Gibbons (Eds), New York, Oxford University Press, 260 pp.
- Kidston J, Tashetto AS, Thompson DWJ, England MH. 2011. The influence of Southern Hemisphere sea-ice extent on the latitude of the mid-latitude jet stream. *Geophys. Res. Lett.* **38**: L15804, DOI: 10.1029/2011GL048056.
- Kodama YM. 1992. Large-scale common features of sub-tropical precipitation zones (the Baiu Frontal Zone, the SPCZ, and the SACZ). Part I: Characteristics of subtropical frontal zones. *J. Meteorol. Soc. Jpn.* **70**: 813–835.
- Kushnir Y, Robinson WA, Blade I, Hall NMJ, Peng S, Sutton R. 2002. Atmospheric GCM response to extratropical SST anomalies: Synthesis and evaluation. *J. Climate* **15**: 2233–2256.
- Lefebvre W, Goosse H. 2008. An analysis of the atmospheric processes driving the large-scale winter sea ice variability in the Southern Ocean. *J. Geophys. Res.* **113**(2): 1–15, DOI: 10.1029/2006JC004032.
- Lemke P, Trinkl EW, Hasselmann K. 1980. Stochastic dynamic analysis of polar sea ice variability. *J. Phys. Oceanogr.* **10**: 2100–2120.
- Lindzen RS, Farrell B. 1980. A simple approximate result for the maximum growth rate of baroclinic instabilities. *J. Atmos. Sci.* **37**: 1648–1654.
- Liu J, Curry JA, Martinson DG. 2004. Interpretation of recent Antarctic sea ice variability. *Geophys. Res. Lett.* **31**(2): L02205, 1–4, DOI: 10.1029/2003GL018732.
- Marengo JA, Liebmann B, Kousky V, Filizola N, Wainer I. 2001. On the onset and end of the rainy season in the Brazilian Amazon basin. *J. Climate* **14**: 833–852.
- Mann H. 1945. Nonparametric tests against trends. *Econometrica* **13**: 245–259.
- Marengo JA, Soares WR, Saulo AC, Nicolini M. 2004. Climatology of the low-level jet east of the Andes as derived from the NCEP–NCAR reanalyses: characteristics and temporal variability. *J. Climate* **17**: 2261–2280.

- Marshall GJ. 2003. Trends in the Southern Annular Mode from observations and reanalyses. *J. Climate* **16**: 4134–4143.
- Marshall GJ, Stott PA, Turner J, Connolley WM, King JC, Lachlan-Cope TA. 2004. Causes of exceptional atmospheric circulation changes in the Southern Hemisphere. *Geophys. Res. Lett.* **31**: L14205, 1–4, DOI: 10.1029/2004GL019952.
- Matthewman NJ, Magnusdottir G. 2011. Observed interaction between sea ice and the Western Pacific Pattern on intraseasonal time scales. *J. Climate* **24**: 5031–5042.
- Monaghan AJ, Bromwich DH, Chapman W, Comiso JC. 2008. Recent variability and trends of Antarctic near-surface temperature. *J. Geophys. Res.* **113**(4): 1–21, DOI: 10.1029/2007JD009094.
- Nogués-Paegle J, Mo KC. 1997. Alternating wet and dry conditions over South America during summer. *Mon. Weather Rev.* **125**: 279–291.
- O'Donnell R, Lewis N, McIntyre S, Condon J. 2011. Improved methods for PCA-based reconstructions: case study using the Steig *et al.* (2009) Antarctic temperature reconstruction. *J. Climate* **24**: 2099–2115.
- Raphael MN, Hobbs W, Wainer I. 2011. The effect of Antarctic sea ice on the Southern Hemisphere atmosphere during the southern summer. *Climate Dynam.* **36**: 1403–1417.
- Rayner NA, Parker DE, Horton EB, Folland CK, Alexander LV, Rowell DP, Kent EC, Kaplan A. 2003. Global analyses of sea surface temperature, sea ice, and night marine air temperature since the late nineteenth century. *J. Geophys. Res.* **108**(14): 1–29, DOI: 10.1029/2002JD002670.
- Renwick JA. 2002. Southern Hemisphere circulation and relations with sea ice and sea surface temperature. *J. Climate* **15**: 3058–3068.
- Ropelewski CF, Halpert MS. 1987. Global and regional scale precipitation patterns associated with the El Niño/Southern Oscillation. *Mon. Weather Rev.* **115**: 1606–1626.
- Screen JA, Simmonds I. 2012. Half-century air temperature change above Antarctica: observed trends and spatial reconstructions. *J. Geophys. Res.* **117**(16): 1–19, DOI: 10.1029/2012JD017885.
- Silvestri GE, Vera CS. 2003. Antarctic Oscillation signal on precipitation anomalies over southeastern South America. *Geophys. Res. Lett.*, DOI: 10.1029/2003GL018277.
- Silvestri GE, Vera CS. 2009. Nonstationary impacts of the Southern Annular Mode on Southern Hemisphere climate. *J. Climate* **22**: 6142–6148.
- Stammerjohn SE, Martinson DG, Smith RC, Yuan X, Rind D. 2008. Trends in Antarctic annual sea ice retreat and advance and their relation to ENSO and Southern Annular Mode variability. *J. Geophys. Res.*, DOI: 10.1029/2007JC004269.
- Steig EJ, Schneider DP, Rutherford SD, Mann ME, Comiso JC, Shindell DT. 2009. Warming of the Antarctic ice-sheet surface since the 1957 International Geophysical Year. *Nature* **457**: 459–463.
- Thompson DWJ, Solomon S. 2002. Interpretation of recent Southern Hemisphere climate change. *Science* **296**: 895–899.
- Thompson DWJ, Wallace JM, Hegerl GC. 2000. Annular modes in the extratropical circulation. Part II: Trends. *J. Climate* **13**: 1018–1036.
- Turner J, Overland J. 2009. Contrasting climate change in the two polar regions. *Polar Res.* **28**: 146–164.
- Turner J, Colwell SR, Marshall GJ, Lachlan-Cope TA, Carleton AM, Jones PD, Lagun V, Iagovkina S. 2005. Antarctic climate change during the last 50 years. *Int. J. Climatol.* **25**: 279–294.
- Turner J, Comiso JC, Marshall GJ, Lachlan-Cope TA, Bracegirdle T, Maksym T, Meredith MP, Wang Z, Orr A. 2009. Non-annular atmospheric circulation change induced by stratospheric ozone depletion and its role in the recent increase of Antarctic sea ice extent. *Geophys. Res. Lett.* **28**(2): 146–164, DOI: 10.1029/2009GL037524.
- Vaughan D, Marshall G, Connolley W, Parkinson C, Mulvaney R, Hodgson D, King J, Pudsey CJ, Turner J. 2003. Recent rapid regional climate warming on the Antarctic Peninsula. *Clim. Change* **60**: 243–274.
- Vera CS, Higgins W, Amador J, Ambrizzi T, Garreaud R, Gochis D, Gutzler D, Lettenmaier D, Marengo J, Mechoso CR, Nogués-Paegle J, Silva Dias PD, Zhang C. 2006. Toward a unified view of the American Monsoon Systems. *J. Climate* **19**: 4977–5000.
- Viale M, Núñez MN. 2011. Climatology of winter orographic precipitation over the subtropical central Andes and associated synoptic and regional characteristics. *J. Hydrometeorol.* **12**: 481–507.
- Xie P, Arkin PA. 1997. Global precipitation: a 17-year monthly analysis based on gauge observations, satellite estimates, and numerical model outputs. *Bull. Am. Meteorol. Soc.* **78**: 2539–2558.
- Zhang J. 2007. Increasing Antarctic sea ice under warming atmospheric and oceanic conditions. *J. Climate* **20**: 2515–2529.